\



SU(3) spin-orbit coupled fermions in an optical lattice

Xiaofan Zhou(周晓凡), Gang Chen(陈刚), and Suo-Tang Jia(贾锁堂)

Citation: Chin. Phys. B, 2022, 31 (**1**): 017102. DOI: 10.1088/1674-1056/ac11dc
Journal homepage: http://cpb.iphy.ac.cn; http://iopscience.iop.org/cpb

What follows is a list of articles you may be interested in

Magnetic impurity in hybrid and type-II nodal line semimetals

Xiao-Rong Yang(杨晓容), Zhen-Zhen Huang(黄真真), Wan-Sheng Wang(王万胜), and Jin-Hua Sun(孙金华)
Chin. Phys. B, 2021, 30 (**6**): 067103. DOI: 10.1088/1674-1056/abfa02

Influence of thickness on current-induced magnetization switching in $L1_0$-FePt single layer

Shi-Qi Zheng(郑诗琪), Kang-Kang Meng(孟康康), Zhen-Guo Fu(付振国), Ji-Kun Chen(陈吉堃), Jun Miao(苗君), Xiao-Guang Xu(徐晓光), and Yong Jiang(姜勇)
Chin. Phys. B, 2021, 30 (**10**): 107101. DOI: 10.1088/1674-1056/ac0a62

Two-dimensional hexagonal Zn_3Si_2 monolayer: Dirac cone material and Dirac half-metallic manipulation

Yurou Guan(官雨柔), Lingling Song(宋玲玲), Hui Zhao(赵慧), Renjun Du(杜仁君), Liming Liu(刘力铭), Cuixia Yan(闫翠霞), Jinming Cai(蔡金明)
Chin. Phys. B, 2020, 29 (**8**): 087103. DOI: 10.1088/1674-1056/ab943a

Giant interface spin-orbit torque in NiFe/Pt bilayers

Shu-Fa Li(李树发), Tao Zhu(朱涛)
Chin. Phys. B, 2020, 29 (**8**): 087102. DOI: 10.1088/1674-1056/ab9292

Global phase diagram of a spin-orbit-coupled Kondo lattice model on the honeycomb lattice

Xin Li(李欣), Rong Yu(俞榕), Qimiao Si
Chin. Phys. B, 2019, 28 (**7**): 077102. DOI: 10.1088/1674-1056/28/7/077102

SU(3) spin–orbit coupled fermions in an optical lattice

Xiaofan Zhou(周晓凡)[1,2,†], Gang Chen(陈刚)[1,2,3], and Suo-Tang Jia(贾锁堂)[1,2]

[1] *State Key Laboratory of Quantum Optics and Quantum Optics Devices, Institute of Laser Spectroscopy, Shanxi University, Taiyuan* 030006, *China*

[2] *Collaborative Innovation Center of Extreme Optics, Shanxi University, Taiyuan* 030006, *China*

[3] *Collaborative Innovation Center of Light Manipulations and Applications, Shandong Normal University, Jinan* 250358, *China*

(Received 19 April 2021; revised manuscript received 23 June 2021; accepted manuscript online 7 July 2021)

We propose a scheme to realize the $SU(3)$ spin–orbit coupled three-component fermions in an one-dimensional optical lattice. The topological properties of the single-particle Hamiltonian are studied by calculating the Berry phase, winding number and edge state. We also investigate the effects of the interaction on the ground-state topology of the system, and characterize the interaction-induced topological phase transitions, using a state-of-the-art density-matrix renormalization-group numerical method. Finally, we show the typical features of the emerging quantum phases, and map out the many-body phase diagram between the interaction and the Zeeman field. Our results establish a way for exploring novel quantum physics induced by the SOC with $SU(N)$ symmetry.

Keywords: spin–orbit coupling, topological phase transition, optical lattice

PACS: 71.70.Ej, 64.70.Tg, 37.10.Jk **DOI:** 10.1088/1674-1056/ac11dc

1. Introduction

Spin–orbit coupling (SOC) plays a key role for several condensed-matter phenomena, such as quantum spin-Hall effect[1–3] and topological insulators,[4–7] and it is also crucial for spintronic devices.[8] The recent experimental realizations of the synthetic SOC in ultracold quantum gases[9–21] provide an ideal platform to investigate quantum many-body physics under a gauge field, in which a lot of parameters can be precisely controlled. In cold-atom systems, the hyperfine states of the alkaline atoms and the clock states of the alkaline-earth(-like) atoms have been treated as the internal degrees of freedom of atoms.[22–26] Coupling the hyperfine (clock) states through synthetic gauge fields by the two-photon (single-photon) process, the SOC has been implemented.[27–32]

The experiments in a gas of ^{87}Rb atoms have succeeded in implementing SOC on spin-1 Bose–Einstein condensates (BECs),[33,34] thus paving the way towards the exploration of the interplay between the spinor character and the SOC in determining the novel quantum phases of the system. For example, the interesting magnetic physics have been observed on $SU(2)$ SOC in spin-1 BECs.[35–40] For $SU(2)$ SOC, the hyperfine states $|-1,0,1\rangle$ are coupled in forms $|-1\rangle \leftrightarrow |0\rangle$ and $|0\rangle \leftrightarrow |1\rangle$ by couple two-photon Raman process, with the coupling $|-1\rangle \leftrightarrow |1\rangle$ missing. After considering the coupling $|-1\rangle \leftrightarrow |1\rangle$, the $SU(2)$ SOC will be extended to the $SU(3)$ SOC. Mathematically, the $SU(2)$ spin-1 matrices only include three spin-1 vectors S^σ ($\sigma = x,y,z$). However, there exist not only three spin-1 vectors but also spin-1 tensors $N^{\sigma\acute{\sigma}} = (S^\sigma S^{\acute{\sigma}} + S^{\acute{\sigma}} S^\sigma)/2 - \delta_{\sigma\acute{\sigma}} S^2/3$ in the $SU(3)$ spin-1 matrices. The $SU(2)$ SOC system always has trivial topology. However, the $SU(3)$ SOC involves all the pairwise couplings between the three internal states, and has no analog in ordinary condensed matter systems, hence it may lead to new quantum phases and topological defects.[41–45]

In this paper, we propose an experimental scheme for realizing an $SU(3)$ SOC of fermions in a one-dimensional optical lattice. For single-particle Hamiltonian, the bulk topological physics can be characterized by the Berry phases of the bands and the winding numbers. The local distribution of the edge states inside the band gap under open boundary condition exhibits the bulk-boundary correspondence of the topology. We discuss the interaction-induced topological phase transition via the state-of-the-art density-matrix renormalization-group (DMRG) numerical method.[46,47] By calculating the entanglement spectrum, entanglement entropies, energy gaps and magnetic order, we find three topological phase transitions. We then clearly show the three many-body quantum phases, i.e., two topological insulators and a charge density wave phase, by the density profile and edge-model density profile.

The work is organized as follows. In Section 2, we present the experimental setup and give the effective Hamiltonian. We analyze the topological properties of the single-particle case in Section 3. We study the interaction-induced topological phase transition and show the many-body phase diagram in Section 4. The conclusions are given in Section 5.

2. Model and Hamiltonian

We consider a quasi-1D cold atomic gas of alkaline atoms trapped in an optical lattice potential along the axial direction,

†Corresponding author. E-mail: zhouxiaofan@sxu.edu.cn

© 2022 Chinese Physical Society and IOP Publishing Ltd

$V^1_{\rm lat}(x) = -V_0\cos^2(k_{\rm L}x)$, with $k_{\rm L} = 2\pi/\lambda_{\rm L}$ and tightly confined in the transverse directions, as shown in Fig. 1(a). We use three stand wave lasers $\Omega_{1,2,3}$ along x-direction with the same Rabi frequency $\Omega_{1,2,3} = \Omega_0\sin(k_{\rm R}x+\varphi)$ ($k_{\rm R} = 2\pi/\lambda_{\rm R}$), but different polarizations (σ,π,σ) to couple the excited states $|e\rangle$ and the ground states $|g_\sigma\rangle$ ($\sigma = \uparrow,0,\downarrow$), respectively, as shown in Fig. 1(b). We set $k_{\rm R} = k_{\rm L}/2$ to get the special SOC. The Raman coupling along the x-direction is $M^x_{\sigma\acute{\sigma}}(x) = \frac{\Omega^*_\sigma\Omega_{\acute{\sigma}}}{\Delta} = (\Omega_0^2/\Delta)\sin^2(k_{\rm R}x+\varphi)$ ($\sigma = \uparrow,0,\downarrow$). Three plane wave Raman lasers along the y-direction with the same Rabi frequency $\Omega_0 e^{\pm iky}$ are applied to make the Raman coupling $M^y_{\sigma\acute{\sigma}}(x) = -\Omega_0^2/2\Delta$. The total Raman coupling $M_{\sigma\acute{\sigma}}(x) = M^x_{\sigma\acute{\sigma}}(x) + M^y_{\sigma\acute{\sigma}}(x) = (\Omega_0^2/2\Delta)\cos(k_{\rm L}x+2\varphi)$. Here, we set the phase $\varphi = -\pi/4$, thus the total Raman coupling $M_{\sigma\acute{\sigma}}(x) = (\Omega_0^2/2\Delta)\sin(k_{\rm L}x)$. The three stand wave Raman lasers along the x-direction support the lattice potentials $V^\sigma_{\rm Ram}(x) = 2|\Omega_0\sin(k_{\rm R}x+\varphi)|^2/\Delta$ for three spin states $|g_\sigma\rangle$ ($\sigma = \uparrow,0,\downarrow$). Another lattice potential $V^2_{\rm lat}(x) = -V^\sigma_{\rm Ram}(x)$ is applied to offset the potential induced by the stand wave Raman lasers. Eliminating the excited state yields the effective Hamiltonian

$$\begin{aligned} H_{\rm eff} =& \sum_\sigma\left[\frac{p_x^2}{2m} + V^1_{\rm lat}(x) + \Gamma_z\tau_z\right]|g_\sigma\rangle\langle g_\sigma| \\ &+ [M_{\sigma\acute{\sigma}}(x)|g_\sigma\rangle\langle g_{\acute{\sigma}}| + {\rm H.c.}], \end{aligned} \tag{1}$$

where p_x is the momentum operator, $\Gamma_z = \hbar\delta$, δ is the two-photo detuning. Using single-band approximation, the tight-binding model Hamiltonian can be written as

$$\begin{aligned} H_{\rm TB} =& -t_{\rm s}\sum_{\langle i,j\rangle,\sigma}\hat{c}^\dagger_{i\sigma}\hat{c}_{j\sigma} + \Gamma_z\sum_i(\hat{n}_{i\uparrow} - \hat{n}_{i\downarrow}) \\ &+ t^{ij}_{\rm so}\sum_{\langle i,j\rangle\sigma,\acute{\sigma}}(\hat{c}^\dagger_{i\sigma}\hat{c}_{j\acute{\sigma}} + {\rm H.c.}), \end{aligned} \tag{2}$$

where

$$\begin{aligned} -t_{\rm s} &= \int {\rm d}x\phi^i_\sigma(x)\left[\frac{p_x^2}{2m} + V^1_{\rm lat}(x)\right]\phi^{i+1}_\sigma(x), \\ t^{ij}_{\rm so} &= \int {\rm d}x\phi^i_\sigma(x)M_{\sigma\sigma'}(x)\phi^{i+1}_{\sigma'}(x). \end{aligned}$$

Here, ϕ^i_σ is the lowest-band Wannier function on the ith site.

The interaction of the system we consider is

$$H_{\rm int} = U\sum_{i,\sigma,\acute{\sigma}}\hat{n}_{i\sigma}\hat{n}_{i\acute{\sigma}}, \tag{3}$$

in which the interaction strength U can be tuned via the external magnetic field through the Feshbach resonance[48] and the strength of the confine optical lattices.[49]

Since the time-reversal, particle-hole, and chiral symmetries are broken, the topological insulator of $H_{\rm TB}$ belongs to the unitary symmetry class A (unitary) of the Altland–Zirnbauer classification and is characterized by a $\mathbb{Z}$ invariant.[50–53] In the presence of weak interaction, the topological insulator with the $\mathbb{Z}$ invariant still exists since the generalized inversion symmetry remains.[54]

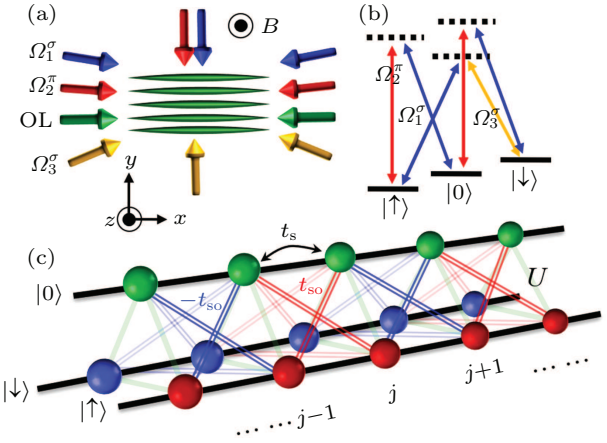


Fig. 1. (a) Schematics of the system setup. Green arrows represent the 1D optical lattice along x-direction. Yellow, blue and red arrows represent three Raman lasers. (b) Energy level and the Raman processing. Ω_1, Ω_2 and Ω_3 couple the ground states $|g_\sigma\rangle$ ($\sigma = \uparrow,0,\downarrow$) to the excited states to achieve the two-photon Raman process. The polarizations of $\Omega_{1,2,3}$ are σ,π,σ, respectively. (c) Schematic picture of the tight-binding model. Here, $t_{\rm s}$ is the spin-conserved hopping between neighboring sites, $t_{\rm so}$ is the spin-flip hopping between neighboring sites, and U is the on-site interaction.

3. Single-particle physics

For single-particle Hamiltonian, one usually fourier transform the real-space Hamiltonian into momentum-space, due to the fact that the momentum k is a good quantum number. Firstly, we rewrite the Hamiltonian (2) as

$$\begin{aligned} H_{\rm TB} =& -t_{\rm s}\sum_{i,\sigma}\left[\hat{c}^\dagger_{{\rm A}i\sigma}\hat{c}_{{\rm B}i\sigma} + \hat{c}^\dagger_{{\rm B}i\sigma}\hat{c}_{{\rm A}(i+1)\sigma} + {\rm H.c.}\right] \\ &+ \Gamma_z\sum_i(\hat{n}_{i\uparrow} - \hat{n}_{i\downarrow}) + t_{\rm so}\sum_{i,\sigma,\acute{\sigma}}(\hat{c}^\dagger_{{\rm A}i\sigma}\hat{c}_{{\rm B}i\acute{\sigma}} + {\rm H.c.}) \\ &- t_{\rm so}\sum_{i,\sigma,\acute{\sigma}}[\hat{c}^\dagger_{{\rm B}i\sigma}\hat{c}_{{\rm A}(i+1)\acute{\sigma}} + {\rm H.c.}], \end{aligned} \tag{4}$$

where $t_{\rm so} = |\int {\rm d}x\phi^i_\sigma(x)M_{\sigma\sigma'}(x)\phi^{i+1}_{\sigma'}(x)|$, and $t^{ij}_{\rm so} = (-1)^i t_{\rm so}$. This Hamiltonian describes an effective lattice in which there are two subsites A and B for one cell, as shown in Fig. 1(c).

Fourier transform the real-space operators with spin label σ and subsite labels A and B into the momentum-space,

$$\begin{aligned} \hat{c}^\dagger_{{\rm A}i\sigma} &= \sum_k e^{-ikX_{{\rm A}i}}\hat{c}^\dagger_{{\rm A}k\sigma}, \quad \hat{c}_{{\rm A}i\sigma} = \sum_k e^{ikX_{{\rm A}i}}\hat{c}_{{\rm A}k\sigma}, \\ \hat{c}^\dagger_{{\rm B}i\sigma} &= \sum_k e^{-ikX_{{\rm B}i}}\hat{c}^\dagger_{{\rm B}k\sigma}, \quad \hat{c}_{{\rm B}i\sigma} = \sum_k e^{ikX_{{\rm B}i}}\hat{c}_{{\rm B}k\sigma}, \end{aligned}$$

in which $X_{{\rm B}i} - X_{{\rm A}i} = a$, $X_{{\rm A}(i+1)} - X_{{\rm B}i} = a$, and a is the lattice constant. Thus the real-space Hamiltonian (4) can be written in momentum-space on the basis of AB cell $\otimes$ σ (i.e. $\Psi^\dagger = [\hat{c}^\dagger_{{\rm A}k\uparrow}\ \hat{c}^\dagger_{{\rm B}k\uparrow}\ \hat{c}^\dagger_{{\rm A}k0}\ \hat{c}^\dagger_{{\rm B}k0}\ \hat{c}^\dagger_{{\rm A}k\downarrow}\ \hat{c}^\dagger_{{\rm B}k\downarrow}]$),

$$H_k = \begin{bmatrix} \Gamma_z & C & 0 & D & 0 & D \\ C & \Gamma_z & D^* & 0 & D^* & 0 \\ 0 & D & 0 & C & 0 & D \\ D^* & 0 & C & 0 & D^* & 0 \\ 0 & D & 0 & D & -\Gamma_z & C \\ D^* & 0 & D^* & 0 & C & -\Gamma_z \end{bmatrix}, \tag{5}$$

with $C = -2\cos(k)t_{\rm s}$, and $D = 2{\rm i}\sin(k)t_{\rm so}$.

3.1. $\Gamma_z = 0$

When $\Gamma_z = 0$, the momentum-space Hamiltonian (5) can be diagonalized analytically to get the eigenvalues $E_n(k)$ with band index n, as shown in Fig. 2(a). The lowest and the second bands are gapless. The second and third bands are fully degenerate. It is hard to explore the band topology. Diagonalizing the tight-binding Hamiltonian Eq. (2) under open boundary condition, we can obtain the energy spectrum as a function of the number of states. There exist four-fold degenerate zero-energy edge states inside the third and fourth bands, as shown in Fig. 2(b).

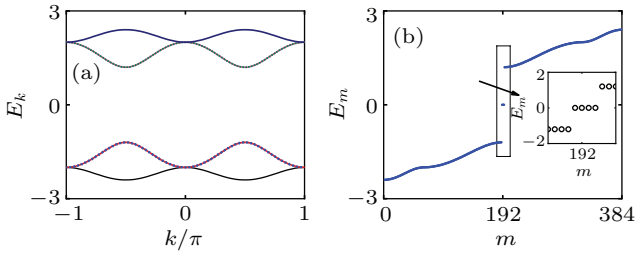


Fig. 2. (a) The dispersion under periodic boundary conditions, and (b) the dispersion under open boundary conditions. For all subfigures, we have $t_{so}/t_s = 0.6$, $\Gamma_z/t_s = 0$ and $L = 128$.

In order to clearly show the band topology, we block diagonalize the momentum-space Hamiltonian (5) in basis $\overline{\Psi}^\dagger = \left[\hat{c}^\dagger_{k\Uparrow}\ \hat{c}^\dagger_{k0}\ \hat{c}^\dagger_{k\Downarrow}\right]$, in which $\hat{c}^\dagger_{k\xi} = [\hat{c}^\dagger_{ak\xi}, \hat{c}^\dagger_{bk\xi}]$ ($\xi = \Uparrow, 0, \Downarrow$). The operators in the basis $\overline{\Psi}$ are composed of operators in the basis Ψ, $\hat{c}^\dagger_{a(b)\xi} = \sum_\sigma \alpha_\sigma \hat{c}^\dagger_{A\sigma} + \beta_\sigma \hat{c}^\dagger_{B\sigma}$, with α_σ and β_σ being the spin-dependent complex numbers. Then, we can obtain a new Hamiltonian H'_k,

$$H'_k = \begin{bmatrix} H'_{\Uparrow k} & 0 & 0 \\ 0 & H'_{0k} & 0 \\ 0 & 0 & H'_{\Downarrow k} \end{bmatrix}, \tag{6}$$

where $H'_{\Uparrow k} = h^{\Uparrow}_x \sigma_x + h^{\Uparrow}_y \sigma_y$, with $h^{\Uparrow}_x \approx 1.5\cos(k)t_s - 1.3\sin(k)t_{so}$ and $h^{\Uparrow}_y \approx -1.3\cos(k)t_s - 1.5\sin(k)t_{so}$. $H'_{0k} \approx h^0_y \sigma_y + h^0_z \sigma_z$, with $h^0_y = -4\sin(k)t_{so}$ and $h^0_z = 2\cos(k)t_s$. $H'_{\Downarrow k} = h^{\Downarrow}_x \sigma_x + h^{\Downarrow}_y \sigma_y$, with $h^{\Downarrow}_x \approx -1.5\cos(k)t_s - 1.3\sin(k)t_{so}$ and $h^{\Downarrow}_y \approx 1.3\cos(k)t_s - 1.5\sin(k)t_{so}$. After analyzing the symmetry of the H'_k, we find that $H'_{\Uparrow k}$, H'_{0k}, and $H'_{\Downarrow k}$ have the chiral symmetry. We calculate the winding number to character the topology, which can be define as

$$\omega_\xi = -\frac{1}{2\pi}\int \mathrm{d}k \cdot \left[\boldsymbol{h}_\xi(k) \times \frac{\partial \boldsymbol{h}_\xi(k)}{\partial k}\right], \tag{7}$$

with flavors $\xi = \Uparrow, 0, \Downarrow$. Figure 3 shows the windings of $\boldsymbol{h}_\xi(k)$. Numerically, the winding number $\omega_\Uparrow = 1$, $\omega_0 = -1$ and $\omega_\Downarrow = -1$.

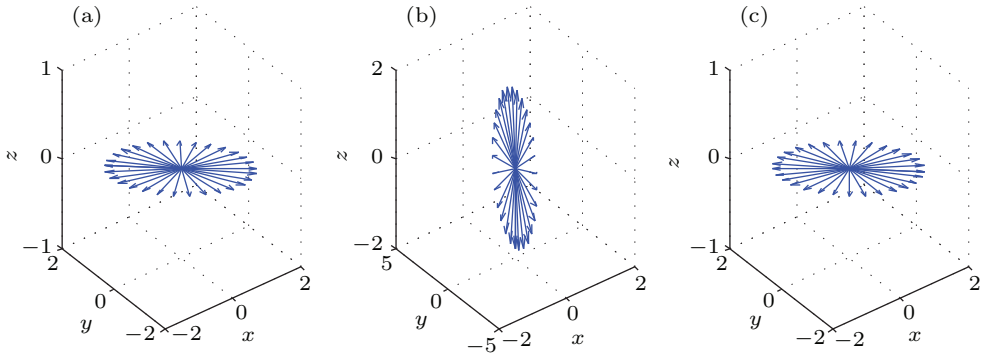


Fig. 3. (a) $\boldsymbol{h}_\Uparrow(k)$, (b) $\boldsymbol{h}_0(k)$, and (c) $\boldsymbol{h}_\Downarrow(k)$. For all subfigures, we have $t_{so}/t_s = 0.6$ and $\Gamma_z/t_s = 0$.

We fourier transform the block diagonalized Hamiltonian (6) into real-space. The real-space effective Hamiltonian can be written as

$$\begin{aligned} H'_{TB} = & \sum_j A\hat{c}^\dagger_{aj\Uparrow}\hat{c}_{bj+1\Uparrow} + B\hat{c}^\dagger_{aj+1\Uparrow}\hat{c}_{bj\Uparrow} + \text{H.c.} \\ & + 2t_{so}\left(-\hat{c}^\dagger_{aj0}\hat{c}_{bj+10} + \hat{c}^\dagger_{aj+10}\hat{c}_{bj0} + \text{H.c.}\right) \\ & + t_s\left(\hat{c}^\dagger_{aj0}\hat{c}_{aj+10} + \hat{c}^\dagger_{aj+10}\hat{c}_{aj0} + \text{H.c.}\right) \\ & + C\hat{c}^\dagger_{aj\Downarrow}\hat{c}_{bj+1\Downarrow} + D\hat{c}^\dagger_{aj+1\Downarrow}\hat{c}_{bj\Downarrow} + \text{H.c.}, \end{aligned} \tag{8}$$

where $A = 0.75t_s + \mathrm{i}0.65t_{so} - \mathrm{i}0.65t_s - 0.75t_{so}$, $B = 0.75t_s - \mathrm{i}0.65t_{so} - \mathrm{i}0.65t_s + 0.75t_{so}$, $C = -0.75t_s + \mathrm{i}0.65t_{so} + \mathrm{i}0.65t_s - 0.75t_{so}$ and $D = -0.75t_s - \mathrm{i}0.65t_{so} + \mathrm{i}0.65t_s + 0.75t_{so}$. The energy spectrum of H'_{TB} under an open boundary condition has six-fold degenerate edge states in zero energy.

3.2. $\Gamma_z > 0$

When $\Gamma_z > 0$, the band gaps are opened. It is convenient to study the band topology by diagonalizing the momentum-space Hamiltonian (5). Diagonalizing Hamiltonian (5), we can reach the Berry phase[55–57]

$$\gamma_n = \mathrm{i}\int \mathrm{d}k \langle \psi_n(k)| \nabla_k |\psi_n(k)\rangle, \tag{9}$$

in which $|\psi_n(k)\rangle$ is the corresponding eigenvectors. The Berry phases γ_n as a function of Γ_z/t_s are shown in Fig. 4(a). When $0 \le \Gamma_z/t_s < 2$, $\gamma_1/\pi = 1$, $\gamma_2/\pi = -1$ and $\gamma_3/\pi = -1$. When $2 < \Gamma_z/t_s < 4$, $\gamma_1/\pi = 1$, $\gamma_2/\pi = -1$ and $\gamma_3/\pi = 1$. When $\Gamma_z/t_s > 4$, $\gamma_1/\pi = 1$, $\gamma_2/\pi = 1$ and $\gamma_3/\pi = 1$. As demon-

strated in Fig. 4(b), we plot the energy spectrum E of tight-binding Hamiltonian (2) under an open boundary condition. When increasing the Zeeman field strength Γ_z/t_s from 0, the zero-energy model splits into two nonzero models, and the gap close at $\Gamma_z/t_s = 2.0$ and then reopen with two zero-energy models in the gap. Further increasing Γ_z/t_s, the gaps inside the second and third bands close and reopen at $\Gamma_z/t_s = 4.0$.

We then clearly show the edge-models of different Γ_z regimes. As demonstrated in Fig. 5, we plot the dispersion and wave function $n(j)$ of the edge-model inside the energy gaps with (a) $\Gamma_z/t_s = 1.0$, (b) $\Gamma_z/t_s = 3.0$, and (c) $\Gamma_z/t_s = 5.0$. For $\Gamma_z/t_s = 1.0$, there are four edge models near the zero energy, with two of them are degenerate, as shown in Fig. 5(a). For $\Gamma_z/t_s = 3.0$, there are two-fold degenerate zero-energy edge models. The edge model are occupied by the atom of 0-component in both sides. Inside the second and third band gap, there are two-fold degenerate edge models, as shown in Fig. 5(b). For $\Gamma_z/t_s = 5.0$, there are two-fold degenerate zero-energy edge models, as shown in Fig. 5(c).

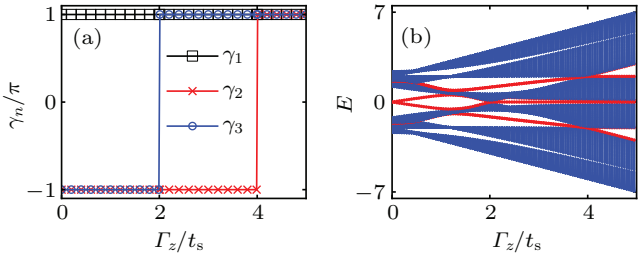


Fig. 4. (a) The Berry phase of each band γ_n under periodic boundary conditions, and (b) the dispersion E under an open boundary condition as a function of Γ_z/t_s. For all the subfigures, we have $t_{so}/t_s = 0.6$ and $L = 128$.

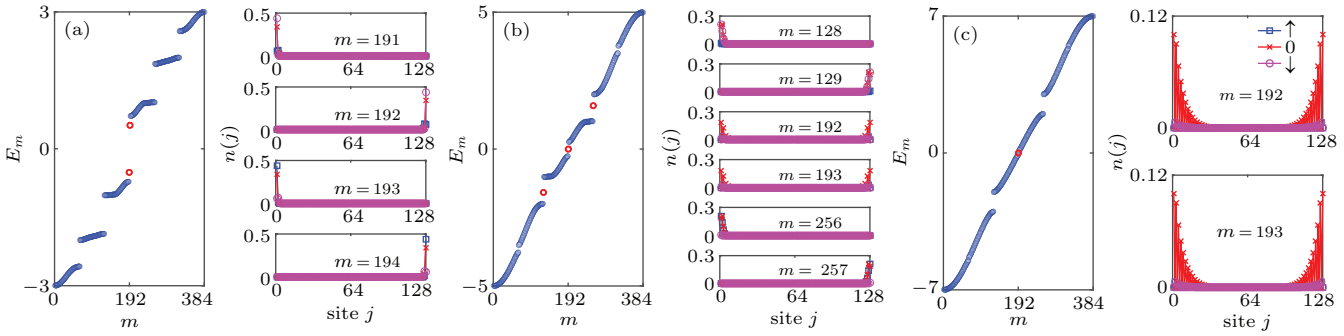


Fig. 5. The dispersion E under open boundary conditions and density profile $n(j)$ of the edge states of (a) $\Gamma_z/t_s = 1.0$, (b) $\Gamma_z/t_s = 3.0$ and (c) $\Gamma_z/t_s = 5.0$. For all the subfigures, we have $t_{so}/t_s = 0.6$ and $L = 128$.

4. Many-body phases

To understand the many-body topological physics of Hamiltonians (2) and (3), we perform the DMRG method to calculate with the model, for which we retain 300 truncated states per DMRG block and perform 20 sweeps with a maximum truncation error $\sim 10^{-7}$. Simply, we focus on band topology when the lowest three bands are fully occupied, which corresponds to the filling $n = N/L = 3/2$ with N being the total atoms number.

The topology of many-body system is reflected in the ground-state degeneracy of the entanglement spectrum, which is defined as[58–64]

$$\xi_i = -\ln(\rho_i). \tag{10}$$

Here, ρ_i is the eigenvalue of the reduced density matrix $\hat{\rho}_L = \mathrm{Tr}_R|\psi\rangle\langle\psi|$, where $|\psi\rangle$ is the many-body ground-state wave function, L and R correspond to the left or the right half of the 1D chain. As the entanglement spectrum ξ_i resembles the energy spectrum of edge excitations, the system is topologically non-trivial if and only if each eigenvalue ξ_i is degenerate.[64] In Fig. 6(a), we show the four lowest levels in the entanglement spectrum as functions of U/t_s. While there is a four-fold degeneracy for the ground states in the entanglement spectrum with $U = 0$, the degeneracy is partially lifted in the presence of weak U. As the degeneracy of the entanglement spectrum is generally equal to the dimension of the irreducible projective representation of the symmetry group, the lift of degeneracy can be understood as the reduction of the projective representations into irreducible ones. The existence and the location of the interaction-driven topological phase transition can be further confirmed by entropy. As demonstrated in Fig. 6(b), sharp features emerge at the critical points in both the second-order Rényi entropy[63–69]

$$S_2 = -\log \mathrm{Tr}(\hat{\rho}_L^2), \tag{11}$$

and the von Neumann entropy

$$S_{vN} = -\mathrm{Tr}_L[\hat{\rho}_L \log \hat{\rho}_L]. \tag{12}$$

In Fig. 6(c) we show the the energy gap E_{gap} for a chain with lattice length $L = 12$ under the periodic boundary condition. The energy gap can be defined as the energy difference between the ground state E_g and the first excited state E_e,

$$E_{gap} = E_e - E_g. \tag{13}$$

As the system crosses the critical point of phase transition, the gap opens. The ground state become from a two-fold degener-

ate phase to a non-degenerate phase. As the system undergoing another phase transition, the gap close and reopen again, which is the typical of a phase transition. The phase transitions can also be organized by the magnetic order

$$\langle S_z\rangle = \sum_j \langle \hat{n}_{j\uparrow} - \hat{n}_{j\downarrow}\rangle. \tag{14}$$

The derivatives of $\mathrm{d}\langle S_z\rangle/\mathrm{d}U$ are divergence at the critical points, as seen in Fig. 6(d). The critical points of the phase transitions in Figs. 6(a)–6(d) match perfectly.

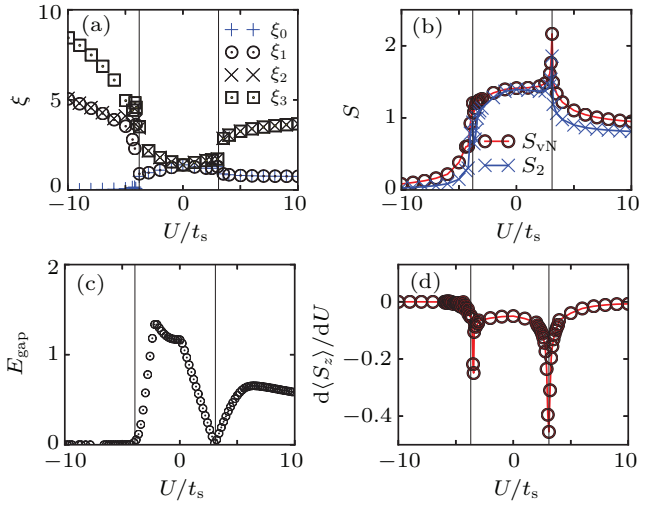


Fig. 6. (a) The lowest four levels in the entanglement spectrum ξ_i ($i = 0, 1, 2, 3$), (b) the von Neumann entropy S_{vN} and the second-order Rényi entropy S_2, (c) the energy gap E_{gap} for a chain with $L = 12$ under the periodic boundary condition, and (d) the first derivative of the magnetic order $\mathrm{d}\langle S_z\rangle/\mathrm{d}U$, as a function of U/t_s. For all the subfigures, we have $t_{so}/t_s = 0.6$, $\Gamma_z/t_s = 1.4$, $n = 3/2$ and $L = 128$.

While the phase boundaries are determined from the above analysis, we further identify the different quantum phases besides the topological phase transitions in Fig. 7. When U/t_s is negatively large, the ground state of the system is a trivial phase, in which left (right) part of the lattice is vacuum, middle of the lattice is charge density wave, and right (left) part is fully occupied, as shown in Fig. 7(a). In this regime, the ground state is two-fold degenerate due to the mirror symmetry of the 1D lattice. This kind of phase is phase-separated (PS) phase. When U/t_s is small and large positive, the ground states are the topological insulators. Here, we use the edge-model density profile to describe the edge states of the topological phases. The edge-model density profile can be defined as

$$\langle \Delta\hat{n}_{j\sigma}\rangle = \langle \hat{n}_{j\sigma}(N+1)\rangle - \langle \hat{n}_{j\sigma}(N)\rangle.$$

For large positive U/t_s, there exists edge state at one side of the lattice, as shown in Fig. 7(b). This topological insulator is two-fold degenerate under the open boundary condition, and is called TI_1. Due to the competition between Zeeman field Γ_z and interaction U, $\langle \hat{n}_\uparrow\rangle \approx 0$, $\langle \hat{n}_0\rangle = 0.5$, and $\langle \hat{n}_\downarrow\rangle \approx 1$. The edge model is occupied by the fermions of $|g_0\rangle$ state, as shown in Figs. 5(b), 5(c) and 7(b). In this case, the Hamiltonian can map to the spin-1/2 SOC and the effects induced by interaction are weak. For small U/t_s, the topological insulator is four-fold degenerate under the open boundary condition, as shown in Fig. 7(c). For each degenerate phase, there are two-component atoms localized at the one side of the lattice. This topological insulator is called TI_0.

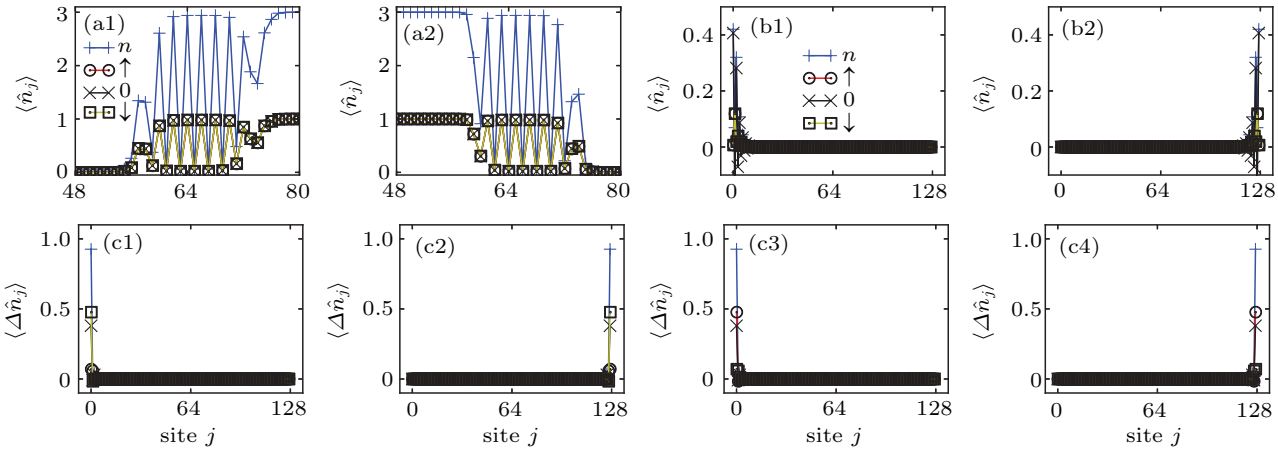


Fig. 7. (a) Density profile $\langle \hat{n}_{j\sigma}\rangle$ of PS with $U/t_s = -7$. The edge-model density profile $\langle \hat{\Delta}n_{j\sigma}\rangle$ of (b) TI_1 with $U/t_s = 6$, and (c) TI_0 with $U/t_s = -1$. For all the subfigures, we have $t_{so}/t_s = 0.6$, $\Gamma_z/t_s = 1.4$, $n = 3/2$ and $L = 128$.

Based on our understanding of the interaction-induced topological phase transitions and the features of the quantum phases, we map out the ground-state phase diagram of Hamiltonians (2) and (3) in the $U/t_s - \Gamma_z/t_s$ plane, as shown in Fig. 8. The phase transition of PS-TI_0 (red line with circle symbol) is of the first order. The phase transitions of PS-TI_1 (black line with square symbol) and TI_0-TI_1 (blue line with diamond symbol) are continuous phase transitions. The order of the phase transition can be determined by the derivative of the ground-state energy.

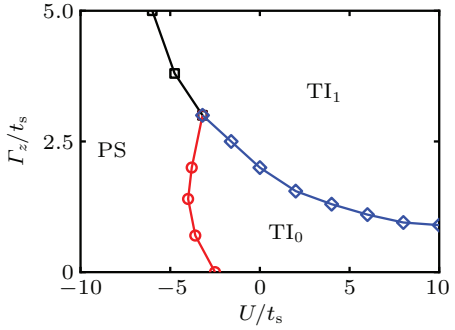


Fig. 8. The phase diagram between U/t_s and Γ_z/t_s, with parameters $t_{so}/t_s = 0.6$ and $n = 3/2$. The red line with circles shows the first-order phase transition. The blue line with diamonds and the black line with squares denote the continuous phase transitions.

5. Conclusions

Before concluding, we briefly discuss how to observe these quantum phases and phase transitions. In cold-atom experiments, the entanglement entropy can be measured using quantum interference of many-body twins of ultracold atoms in optical lattices.[69] The local distributions can be measured by isolating the sites of interest using additional site-resolved potentials.[70] Thus, all the quantum phases and the phase transitions can be observed experimentally.

In conclusion, we have proposed a scheme to realize the $SU(3)$ spin–orbit coupled three-component fermions in a 1D optical lattice. We study the topological properties of single-particle Hamiltonian by calculating the Berry phase, winding number and edge states. We also numerically investigate the effects of interactions on the topological properties of the system by employing the DMRG method. The interaction competing with the Zeeman field can induce PS phase and two topological insulators. We have characterized the interaction-induced topological phase boundaries, and map out the phase diagram. Our results provide a way for exploring many-body quantum physics induced by $SU(N)$ SOC.

Acknowledgements

This work was supported by the National Key R&D Program of China (Grant No. 2017YFA0304203), the Natural National Science Foundation of China (Grant Nos. 11674200, 12074232, and 12004230), the Fund for Shanxi '1331 Project' Key Subjects Construction, and Research Project Supported by Shanxi Scholarship Council of China.

References

[1] Kato Y K, Myers R C, Gossard A C and Awschalom D D 2004 *Science* **306** 1910
[2] König M, Wiedmann S, Brüne C, Roth A, Buhmann H, L W Molenkamp, Qi X L, Zhang S C 2007 *Science* **318** 766
[3] Xiao D, Chang M C and Niu Q 2010 *Rev. Mod. Phys.* **82** 1959
[4] Bernevig B A, Hughes T L, and Zhang S C 2006 *Science* **314** 1757
[5] Hsieh D, Qian D, Wray L, Xia Y, Hor Y S, Cava R J, and Hasan M Z 2008 *Nature* **452** 970
[6] Hasan M Z and Kane C L 2010 *Rev. Mod. Phys.* **82** 3045
[7] Qi X L and Zhang S C 2011 *Rev. Mod. Phys.* **83** 1057
[8] Koralek J D, Weber C P, Orenstein J, Bernevig B A, Zhang S C, Mack S and Awschalom D D 2009 *Nature* **458** 610
[9] Lin Y J, Jimenez-Garcia K and Spielman I B 2011 *Nature* **471** 83
[10] Wang P Yu Z Q, Fu Z, Miao J, Huang L, Chai S, Zhai H and Zhang J 2012 *Phys. Rev. Lett.* **109** 095301
[11] Cheuk L W, Sommer A T, Hadzibabic Z, Yefsa T h, Bakr W S and Zwierlein M W 2012 *Phys. Rev. Lett.* **109** 095302
[12] Zhang J Y, Ji S C, Chen Z, Zhang L, Du Z D, Yan B, Pan G S, Zhao B, Deng Y J, Zhai H, Chen S and Pan J W 2012 *Phys. Rev. Lett.* **109** 115301
[13] Qu C, Hamner C, Gong M, Zhang C and Engels P 2013 *Phys. Rev. A* **88** 021604
[14] Fu Z, Huang L, Meng Z, Wang P, Zhang L, Zhang S, Zhai H, Zhang P and Zhang J 2014 *Nat. Phys.* **10** 110
[15] Ji S C, Zhang J Y, Zhang L, Du Z D, Zheng W, Deng Y J, Zhai H, Chen S and Pan J W 2014 *Nat. Phys.* **10** 314
[16] Olson A J, Wang S J, Niffenegger R J, Li C H, Greene C H and Chen Y P 2014 *Phys. Rev. A* **90** 013616
[17] Huang L, Meng Z, Wang P, Peng P, Zhang S L, Chen L, Li D, Zhou Q and Zhang J 2016 *Nat. Phys.* **12** 540
[18] Meng Z, Huang L, Peng P, Li D, Chen L, Xu Y, Zhang C, Wang P and Zhang J 2016 *Phys. Rev. Lett.* **117** 235304
[19] Wu Z, Zhang L, Sun W, Xu X T, Wang B Z, Ji S C, Deng Y, Chen S, Liu X J and Pan J W 2016 *Science* **354** 83
[20] Sun W, Wang B Z, Xu X T, Yi C R, Zhang L, Wu Z, Deng Y, Liu X J, Chen S and Pan J W 2018 *Phys. Rev. Lett.* **121** 150401
[21] Wang Z Y, Cheng X C, Wang B Z, Zhang J Y, Lu Y Hui, Yi C R, Niu S, Deng Y, Liu X J, Chen S and Pan J W 2021 *Science* **372** 271
[22] Mancini M, Pagano G, Cappellini G, Livi L, Rider M, Catani J, Sias C, Zoller P, Inguscio M, Dalmonte M and Fallani L 2015 *Science* **349** 1510
[23] Stuhl B K, Lu H I, Aycock L M, Genkina D and Spielman I B 2015 *Science* **349** 1514
[24] Zhou X, Pan J S, Yi W, Chen G and Jia S 2017 *Phys. Rev. A* **96** 023627
[25] Yan Y, Zhang S.-L, Choudhury S and Zhou Q 2019 *Phys. Rev. Lett.* **123** 260405
[26] Anderson R P, Trypogeorgos D, Valdés-Curiel A, Liang Q Y, Tao J, Zhao M, Andrijauskas T, Juzeliunas G and Spielman I B 2020 *Phys. Rev. Research* **2** 013149
[27] Liu X J, Liu Z X and Cheng M 2013 *Phys. Rev. Lett.* **110** 076401
[28] Celi A, Massignan P, Ruseckas J, Goldman N, Spielman I B, Juzeliūnas G and Lewenstein M 2014 *Phys. Rev. Lett.* **112** 043001
[29] Zhai H 2015 *Rep. Prog. Phys.* **78** 026001
[30] Livi L F, Cappellini G, Diem M, Franchi L, Clivati C, Frittelli M, Levi F, Calonico D, Catani J, Inguscio M and Fallani L 2016 *Phys. Rev. Lett.* **117** 220401
[31] Wall M L, Koller A P, Li S, Zhang X, Cooper N R, Ye J and Rey A M 2016 *Phys. Rev. Lett.* **116** 035301
[32] Zhou X, Pan J S, Liu Z X, Zhang W, Yi W, Chen G and Jia S 2017 *Phys. Rev. Lett.* **119** 185701
[33] Campbell D L, Price R M, Putra A, Valdés-Curiel A, Trypogeorgos D and Spielman I B 2016 *Nat. Commun.* **7** 10897
[34] Luo X, Wu L, Chen J, Guan Q, Gao K, Xu Z F, You L and Wang R 2016 *Sci. Rep.* **6** 18983
[35] Lan Z. and Öhberg P 2014 *Phys. Rev. A* **89** 023630
[36] Martone G I, Pepe F V, Facchi P, Pascazio S and Stringari S 2016 *Phys. Rev. Lett.* **117** 125301
[37] Natu S S, Li X P and Cole W S 2015 *Phys. Rev. A* **91** 023608
[38] Pixley J H, Natu Stefan S, Spielman I B and Das Sarma S 2016 *Phys. Rev. B* **93** 081101
[39] Sun K, Qu C L, Xu Y, Zhang Y P and Zhang C W 2016 *Phys. Rev. A* **93** 023615
[40] Yu Z Q 2016 *Phys. Rev. A* **93** 033648
[41] Barnett R, Boyd G R, and Galitski V 2012 *Phys. Rev. Lett.* **109** 235308
[42] Graß T, Chhajlany R W, Muschik C A and Lewenstein M 2014 *Phys. Rev. B* **90** 195127
[43] Han W, Zhang X F, Song S W, Saito H, Zhang W, Liu W M and Zhang S G 2016 *Phys. Rev. A* **94** 033629
[44] Han J H, Kang J H and Shin Y 2019 *Phys. Rev. Lett.* **122** 065303
[45] Zhou X, Chen G and Jia S 2020 *Phys. Rev. A* **102** 043313
[46] White S R 1992 *Phys. Rev. Lett.* **69** 2863
[47] Schollwök U 2005 *Rev. Mod. Phys.* **77** 259
[48] Bloch I, Dalibard J and Zwerger W 2008 *Rev. Mod. Phys.* **80** 885

[49] Bergeman T, Moore G M and Olshanii M 2003 *Phys. Rev. Lett.* **91** 163201
[50] Altland A and Zirnbauer M R 1997 *Phys. Rev. B* **55** 1142
[51] Schnyder A P, Ryu S, Furusaki A and Ludwig A W W 2008 *Phys. Rev. B* **78** 195125
[52] Chiu C K, Teo J C Y, Schnyder A P and Ryu S 2016 *Rev. Mod. Phys.* **88** 035005
[53] Ludwig A W W 2016 *Phys. Scr.* **T168** 014001
[54] Morimoto T, Furusaki A and Mudry C 2015 *Phys. Rev. B* **92** 125104
[55] Xiao D, Chang M C and Niu Q 2010 *Rev. Mod. Phys.* **82** 1959
[56] Zak J 1989 *Phys. Rev. Lett.* **62** 2747
[57] Lang L J, Zhang S L and Zhou Q 2017 *Phys. Rev. A* **95** 053615
[58] Zhao J Z, Hu S J and Zhang P 2015 *Phys. Rev. Lett.* **115** 195302
[59] Yoshida T, Peters R, FujimotoS and Kawakami N 2014 *Phys. Rev. Lett.* **112** 196404
[60] Turner A. M, Pollmann F and Berg E 2011 *Phys. Rev. B* **83** 075102
[61] Pollmann F, Turner A M, Berg E and Oshikawa M 2010 *Phys. Rev. B* **81** 064439
[62] Fidkowski L 2010 *Phys. Rev. Lett.* **104** 130502
[63] Flammia S T, A Hamma, Hughes T L and Wen X G 2009 *Phys. Rev. Lett.* **103** 261601
[64] Li H and Haldane F D M 2008 *Phys. Rev. Lett.* **101** 010504
[65] Hastings M B, González I, Kallin A B and Melko R G 2010 *Phys. Rev. Lett.* **104** 157201
[66] Daley A J, Pichler H, Schachenmayer J and Zoller P 2012 *Phys. Rev. Lett.* **109** 020505
[67] Abanin D A and Demler E 2012 *Phys. Rev. Lett.* **109** 020504
[68] Jiang H C, Wang Z H and Balents L 2012 *Nat. Phys.* **8** 902
[69] Islam R, Ma R, Preiss P M, Tai M E, Lukin A, Rispoli M and Greiner M 2015 *Nature* **528** 77
[70] Parsons M F, Mazurenko A, Chiu C. S, Ji G, Greif D and Greiner M 2016 *Science* **353** 1253